

# Active light-controlled frontal ring-opening metathesis polymerization

Received: 9 January 2025

Accepted: 23 June 2025

Published online: 08 July 2025



D. R. Darby<sup>1,3</sup>, A. J. Greenlee<sup>1,2,3</sup>, R. H. Bean<sup>1</sup>, D. C. Fairchild<sup>1</sup>, V. C. Rodriguez<sup>1</sup>,  
A. L. Jansen<sup>1</sup>, S. C. Gallegos<sup>1</sup>, S. P. Ramirez<sup>1</sup>, J. S. Moore<sup>2</sup>,  
S. C. Leguizamon<sup>1</sup>✉ & L. N. Appelhans<sup>1</sup>✉

Frontal ring-opening metathesis polymerization (FROMP) is a promising energy-efficient approach to fabricate polymeric materials. Recent advances have demonstrated FROMP for diverse applications, including additive manufacturing, composites, and foams. However, the characteristic properties of the front are currently controlled primarily by varying the resin composition or the environmental conditions. In this work we present an approach to control FROMP of dicyclopentadiene (DCPD) using photochemical methods. A photobase generator is used to inhibit FROMP of DCPD with UV light while a photosensitizer and co-initiator are used to accelerate FROMP with blue light, enabling orthogonal active photocontrol of front velocity. In addition, photoinhibition-enabled lithographic patterning of frontal polymerizations is demonstrated. Frontal polymerizations are spatially controlled, redirected, and even split into diverging fronts. This work establishes a foundation for advanced control of frontal polymerizations, enabling innovation in traditional and additive manufacturing, as well as emerging processes like morphogenic manufacturing.

In the last two decades, frontal polymerization (FP) has emerged as a useful, energy-efficient technique for the preparation of polymeric materials<sup>1–5</sup>, including fiber-reinforced composites<sup>3,6–9</sup>, nanocomposites<sup>10</sup>, hydrogels<sup>11–13</sup>, and functionally graded polymers<sup>14,15</sup>. In a frontal polymerization system, polymerization is initiated by activation of a latent catalyst through local heating or irradiation and propagates due to the large exotherm generated during polymerization, rather than using an external energy source to drive the reaction<sup>4</sup>. In frontal ring-opening metathesis polymerization (FROMP) (Fig. 1a) this process often results in rapid and near-quantitative conversion of monomer to polymer with minimal energy input, making frontal polymerization an attractive method for the energy-efficient production of polymeric materials<sup>3,4</sup>.

In FROMP, front velocity is controlled by modifying the resin composition, while after initiation, it is regulated by boundary conditions such as substrate temperature, ambient thermal environment, and heat flux at the resin boundaries<sup>4,16,17</sup>. The resin composition influences the heat release rate, which depends on the product of the

intrinsic enthalpy of polymerization and the polymerization reaction rate. The enthalpy of polymerization is determined by the monomer, while the reaction rate is governed by the relative concentrations and activities of monomer, catalyst, and phosphite inhibitor<sup>16,18,19</sup>. Gao et al. introduced a creative approach to controlling front velocity in cyclooctadiene FROMP by incorporating phase-changing micro-particles into the resin<sup>20</sup>. This innovation highlights the complexity of managing front velocity, which is highly sensitive to variables such as resin formulation, part geometry, and substrate or mold material. For applications like direct ink write (DIW) additive manufacturing<sup>3,21</sup>, these sensitivities require careful optimization of process parameters for each specific formulation. To make the additive manufacturing process more robust, the Sottos group developed a self-regulating approach for DIW printing by controlling the resin and substrate temperatures<sup>17</sup>.

Several groups have investigated the photochemical and photo-thermal initiation of FROMP<sup>22–25</sup>. Wavelength orthogonal control of

<sup>1</sup>Sandia National Laboratories, Albuquerque, NM, USA. <sup>2</sup>University of Illinois, Champaign, IL, USA. <sup>3</sup>These authors contributed equally: D. R. Darby, A. J. Greenlee. ✉ e-mail: [sleguiz@sandia.gov](mailto:sleguiz@sandia.gov); [lappelh@sandia.gov](mailto:lappelh@sandia.gov)

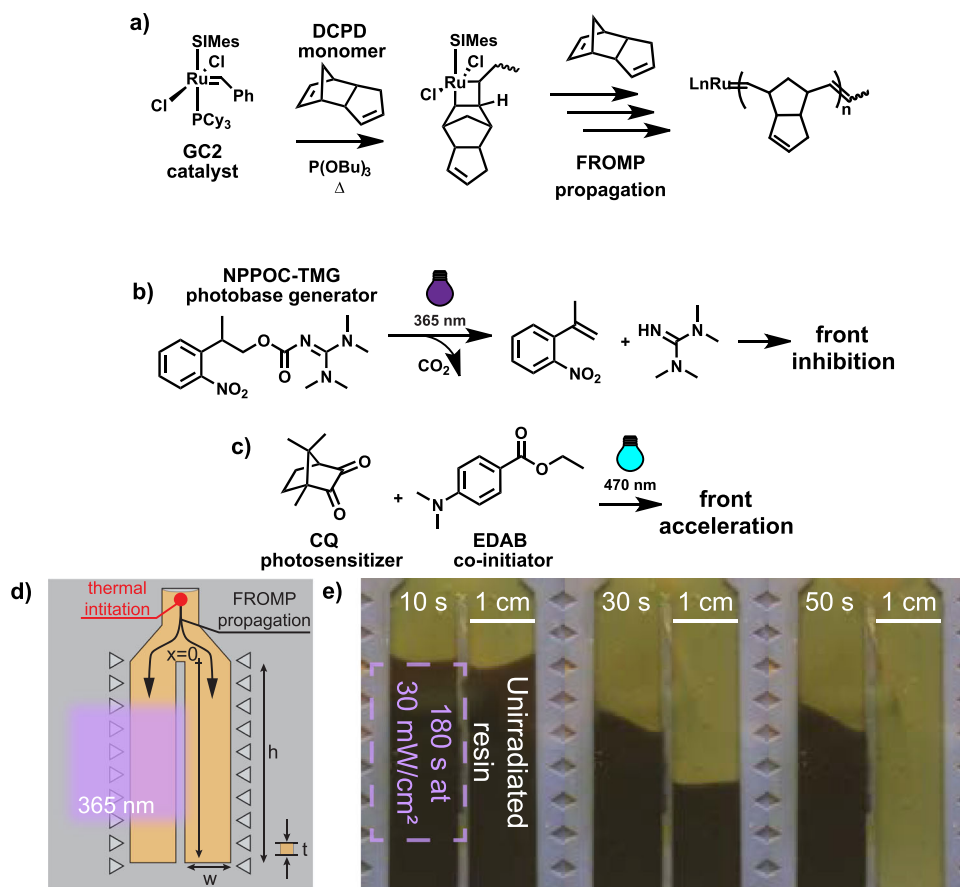


**Fig. 1 | Overview of orthogonal photocontrol system.** **a** ROP with DCPD showing metallacyclobutane intermediate, ring-opening of the cyclopentene is not shown, **b** photoactivation of NPPOC-TMG, for inhibition of FROMP and **c** the photosensitizer system for wavelength orthogonal acceleration of FROMP. **d** Schematic of a 2-channel experiment to compare front velocities with a test and control (unirradiated) channel. **e** Still images of FROMP with photoinhibition in a

2-channel mold. The right channel is unirradiated and propagates to the end of the channel. The left channel is preirradiated with  $30 \text{ mW cm}^{-2}$  light for 180 s and front propagation is arrested on entering the inhibited region. The resin contains 8 mole equivalents of NPPOC-TMG:catalyst and a thermochromic dye to enhance visualization of the front. For scale, the molds have triangular indents spaced 5 mm apart along the edges.

catalyst activity has also been demonstrated for photoinitiated ROP (photoROMP)<sup>26–30</sup> including work by our group which previously demonstrated acceleration of photoROMP for 3D printing using photosensitizers<sup>31,32</sup> as well as selective wavelength-orthogonal olefin metathesis polymerization (SWOMP) using photobase generators and photosensitizers<sup>33</sup>. In this work, we apply similar approaches to FROMP of dicyclopentadiene (DCPD), demonstrating photocontrol of both front velocity and direction despite the high frontal temperatures ( $\sim 130$ – $220^\circ\text{C}$  for DCPD)<sup>34,35</sup> and fast propagation of FROMP. We investigate the effects of photobase generator loading and light intensity on front inhibition and compare the efficacy of inhibition with in situ photobase generation versus preirradiation. We also demonstrate the use of photosensitizer systems for in situ acceleration of the front and develop a resin formulation for wavelength-orthogonal acceleration and inhibition (Fig. 1b,c). Finally, we explore photopatterning of resins utilizing FROMP inhibition to confine frontal polymerization to patterned areas and change the front direction using only light. This work establishes active control over self-propagating reactions, paving the way for spatiotemporal control of FROMP in advanced and morphogenic manufacturing<sup>36,37</sup>.

## Results and discussion

FROMP resins in this work are formulated with monomer, catalyst, and a phosphite inhibitor, to prevent rapid polymerization when the catalyst and monomer are mixed. For all experiments in this work FROMP was thermally initiated, although prior work has demonstrated both

photochemical and photothermal initiation methods can be effective<sup>22–25</sup>. Front velocity is highly dependent on catalyst and phosphite inhibitor concentration and significantly varies batch-to-batch due to small variations in the resin formulation (Supplementary Figs. S1 and S2). To ensure differences due to variations in the formulations were not misattributed as effects of irradiation, two-channel and three-channel molds (Fig. 1d, e; Supplementary Fig. S3), which allow direct comparison of irradiated fronts to an unirradiated control front from the same batch of resin, were used for all photocontrol experiments.

### NPPOC-TMG stability

Amines are well-known to inhibit solution-state ROP polymerizations, although the extent of amine sensitivity depends on both the specific catalyst and the amine<sup>38–42</sup>. Mechanistic work by the Fogg<sup>43–46</sup> group has shown that amine inhibition of N-heterocyclic carbene-substituted Grubbs' catalysts can proceed by abstracting protons from the metallacyclobutane intermediate or by nucleophilic attack at the vinylidene, depending on the substitution and nucleophilicity of the amine. We utilized the photobase generator 2-(2-nitrophenyl)propyl-N-(1,1,3,3-tetramethylguanidiny)l carbamate (NPPOC-TMG)<sup>47</sup> which generates 1,1,3,3-tetramethylguanidine (TMG) upon photoactivation (Fig. 1b). While photoROMP inhibition by NPPOC-TMG was previously demonstrated at room temperature<sup>33</sup>, it was unknown if NPPOC-TMG would be stable or if inhibition would be effective at the elevated temperatures ( $\sim 130$ – $220^\circ\text{C}$ ) and rapid reaction rates of FROMP<sup>4,35,48</sup>.

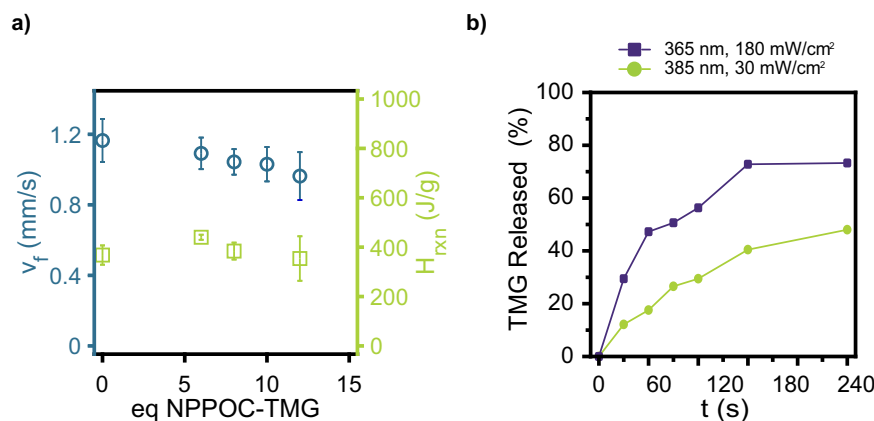


**Fig. 2 | NPPOC-TMG in DCPD resins. a** Front velocity ( $v_f$ ) and polymerization enthalpy ( $H_{rxn}$ ) with standard deviations for unirradiated FROMP resins with varied mol eq. NPPOC-TMG: catalyst, demonstrating a small decrease in  $v_f$  with increasing NPPOC-TMG loading but no statistically significant impact on  $H_{rxn}$  (Supplementary

Table S1 and Figures S6–S8). **b** NPPOC-TMG conversion in DCPD measured by NMR spectroscopy when 1.3 mm thick samples are exposed to 365 nm and 385 nm light for varied preirradiation times.

The thermal stability of neat NPPOC-TMG was assessed by thermogravimetric analysis (TGA) and differential scanning calorimetry (DSC) both of which showed that neat NPPOC-TMG is stable at FROMP temperatures. NMR of NPPOC-TMG samples after DSC to 200 °C showed no evidence of degradation products (Supplementary Figs. S4 and S5).

To determine the stability of NPPOC-TMG under FROMP conditions, FROMP was performed without irradiation on resins containing 6–12 mol eq. of NPPOC-TMG vs catalyst. The resins were frontally polymerized and the front velocities were measured (Fig. 2a). Thermal activation of NPPOC-TMG, or reaction of unactivated NPPOC-TMG with the catalyst, should decrease the observed front velocity due to catalyst deactivation<sup>18</sup>. A small but statistically significant trend of decreasing front velocity with increasing NPPOC-TMG concentration was observed (Fig. 2a, Supplementary Table S1 and Fig. S6). The FROMP front temperature was also measured in unirradiated resin containing 8 mol eq. NPPOC-TMG and found to be -140 °C (Supplementary Fig. S8). The total enthalpy of polymerization showed little change with the addition of NPPOC-TMG below 12 mol eq. (Supplementary Fig. S7), consistent with previous work which showed that lower catalyst loading does not change the total enthalpy although the front velocities decrease<sup>18</sup>. However, at or above 12 equivalents, NPPOC-TMG was observed to have a detrimental effect on front stability and propagation, with fronts in 2-channel experiments frequently spontaneously arresting or failing to propagate after the thermal stimulus was removed, even in the control channel. We conclude that NPPOC-TMG does not undergo significant thermal activation during FROMP, but at high concentrations it does impact front propagation. This could be due to an interaction between unreacted NPPOC-TMG and the catalyst during the initiation or propagation steps of the polymerization or to small amounts of thermally-released TMG which only have a measurable effect on FROMP at high NPPOC-TMG loadings.

Finally, to determine if NPPOC-TMG or TMG have a detrimental effect on the thermomechanical properties of FROMP-polymerized pDCPD, DMA and DSC tests were conducted on polymers with unirradiated and irradiated NPPOC-TMG and with directly added TMG. None of the samples exhibited a significant difference in either  $T_g$  or torsional modulus compared to control specimens (Supplementary Figs. S9–S11), demonstrating that the thermomechanical properties of the FROMP polymers are unaffected by the presence of NPPOC-TMG or released TMG at experimentally relevant concentrations. Future work will evaluate the long-term effects, if any, of residual NPPOC-TMG and TMG on polymer thermomechanical properties, such as  $T_g$ , modulus and toughness, and aging performance.

### NPPOC-TMG photoactivation kinetics

The kinetics of TMG release upon photoactivation of NPPOC-TMG are critical for effective front inhibition, as they directly influence the thermal dynamics of the region just ahead of the frontal boundary. In this region the temperature rises due to heat conduction from the propagating front. This temperature increase, governed by the resin's thermal conductivity and the existing temperature gradient, establishes an elevated temperature zone where polymerization is initiated. For the front to propagate, the heat released by polymerization in this zone must exceed the heat lost to the surrounding medium and resin. The release of TMG inhibits the exothermic polymerization reaction, lowering the heat generation rate and preventing the initiation zone from reaching the critical temperature required for self-sustained propagation. The interplay between the kinetics of TMG release, catalyst deactivation by TMG, resin thermal conductivity, and heat transfer processes ultimately determines how far the front propagates into an irradiated region before being quenched.

To determine the approximate range of NPPOC-TMG needed to inhibit the front the ability of neat TMG to inhibit FROMP was investigated by adding TMG directly to FROMP resins. We found that with >6 mol eq. of TMG relative to catalyst the FROMP front arrested (Supplementary Fig. S13). Based on this we investigated resins with NPPOC-TMG added at 6 mol eq. relative to catalyst and above.

Bowman and coworkers<sup>49</sup> previously studied the photorelease kinetics of NPPOC-TMG. Photoactivation kinetics were expected to be slower in our system due to the ruthenium catalyst, which has significant UV absorption (Supplementary Fig. S12). Photoactivation of NPPOC-TMG was measured directly by NMR and by UV-Vis utilizing an acid-base indicator to determine how much TMG was released at different light intensities and times<sup>49</sup>.

For NMR samples a much higher loading of NPPOC-TMG than used in photocontrol experiments was needed to provide adequate signal for the NPPOC-TMG peaks. For 1.3 mm thick samples in DCPD, irradiating at 180 mW cm<sup>-2</sup> with 365 nm light NPPOC-TMG reached 50% activation after 90 s and 73% after 180 s (Fig. 2b). Unsurprisingly, NPPOC-TMG activation was slower with lower intensity 385 nm light (30 mW cm<sup>-2</sup>), with only 27% activation after 90 s and 40% of the NPPOC-TMG activated after 180 s. The effect of penetration depth was studied and activation was greater for thinner layers of resin. NPPOC-TMG activation kinetics were also studied by UV-Vis in DCPD and dichloroethane (DCE). The UV-Vis results in DCPD were quite similar to the kinetics measured by NMR. Although the initial activation was slightly faster when measured by UV-Vis the activation also plateaued at approximately 70%. In DCE the initial activation rate was similar, but

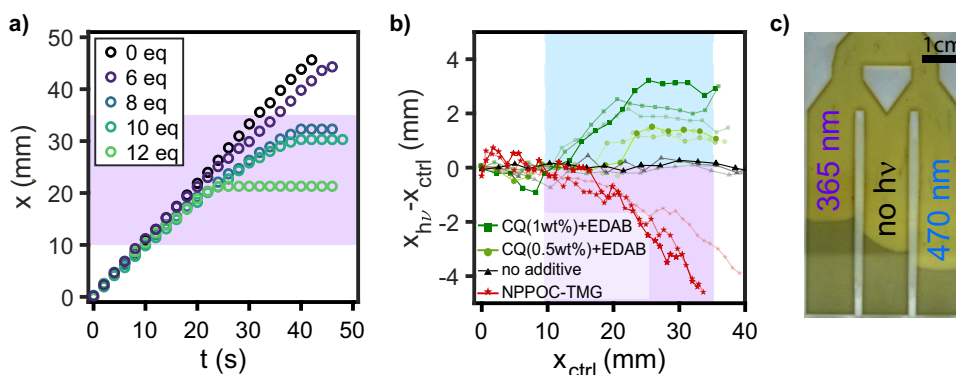


**Fig. 3 | Front inhibition and acceleration.** **a** Representative curves of front position versus time for 2-channel tests with in situ irradiation (365 nm, 180 mW cm<sup>-2</sup>) and varying molar equivalents of NPPOC-TMG:catalyst (0–12 mol eq.). Purple indicates the irradiated region. **b** Inhibition and acceleration in 2-channel tests with NPPOC-TMG (365 nm, 180 mW cm<sup>-2</sup>) and CQ/EDAB (470 nm, 120 mW cm<sup>-2</sup>) at two different loadings. Data from three runs are shown for each formulation, indicated by the different sizes and shades of symbols. The blue and purple shading indicate the irradiated region. The position of the irradiated front relative to the control

(unirradiated) front is tracked by subtracting the control front position from the irradiated front position at time (*t*) and plotting the relative position versus the distance of the control front. Negative values show inhibition and positive values show acceleration. **c** A 3-channel experiment showing in situ orthogonal control of FROMP in a single resin with both NPPOC-TMG (8 mol eq.) and CQ/EDAB (0.5 wt% CQ and 1 wt% EDAB) using 220 mW cm<sup>-2</sup> 365 nm light (left channel, inhibition) and 200 mW cm<sup>-2</sup> 470 nm light (right channel, acceleration). See also Supplementary Movie 2.

the activation proceeded to 95% activation after 180 s. These differences could be due to many factors including solvent effects and differences in light penetration due to the necessity of varying the compositions of the solutions tested for each method (Supplementary Figs. S14–S16 and Tables S2–S4).

We also investigated the main byproduct of NPPOC-TMG activation, 1-nitro-2-(prop-1-en-2-yl)benzene (NO<sub>2</sub>Sty) (Fig. 1b). We found NO<sub>2</sub>Sty has some absorption at 365 nm (Supplementary Fig. S17a) which may contribute to the plateau observed in NPPOC-TMG activation around 70% for 1.3 mm depth experiments. However, in 2-channel experiments with 8 mol eq. NO<sub>2</sub>Sty relative to catalyst the presence of the NO<sub>2</sub>Sty byproduct was not found to have a significant effect on front rate relative to formulations with no photoadditives (Supplementary Fig. S17b), although the average front rate of the irradiated channels with NO<sub>2</sub>Sty was slightly lower than in the control (unirradiated) channels with NO<sub>2</sub>Sty. This suggests that NO<sub>2</sub>Sty may have a slight inhibitory effect on FROMP when irradiated.

### In situ front velocity control

The efficacy of NPPOC-TMG based photoinhibition for in situ control of FROMP front velocity was tested using 2-channel experiments. In these experiments, a light source was turned on as the front passed a designated point in each channel (*x* = 10 mm) and remained on as the front propagated along the channel through the 25 mm irradiation zone (Fig. 1d). Formulations with varying equivalents of NPPOC-TMG vs catalyst were tested with 120, 180, and 228 mW cm<sup>-2</sup> intensity 365 nm light (Fig. 3a) (Supplementary Fig. S18, Supplementary Movie 1).

Representative curves of front position versus time for resins with varying NPPOC-TMG loadings irradiated in situ at 180 mW cm<sup>-2</sup> show that increased NPPOC-TMG increases inhibition and causes the front to arrest earlier in the irradiated region (Fig. 3a). At 6 mol eq. NPPOC-TMG, the front does not typically fully arrest, but FROMP velocity decreases in the irradiated region. Formulations containing ≥8 mol eq. NPPOC-TMG, by contrast, consistently arrest in the irradiated region. Owing to the photorelease efficiency of NPPOC-TMG and the sensitivity of FROMP to small variations in resin formulation, the run-to-run variability of these experiments is relatively high, particularly at low irradiation intensity and lower NPPOC-TMG loading (Supplementary Fig. S18).

Next, we examined in situ acceleration of FROMP with photosensitizers. In previous work<sup>32</sup> we showed that the addition of

photosensitizers can accelerate photoROMP, although the exact mechanism of energy transfer between the photosensitizers and the Ru catalysts continues under investigation. We reasoned that a similar acceleration of FROMP, by increasing the activity of the Ru catalyst, would be possible using photosensitizers and in situ irradiation. A series of photosensitizers were screened with and without ethyl 4-(dimethylamino)benzoate (EDAB) as a co-initiator (Supplementary Figs. S19–S21), demonstrating that several combinations of photosensitizers can accelerate FROMP with 365 nm light, and that EDAB increases the acceleration effect for most photosensitizers. The results of 2-channel acceleration and inhibition experiments using separate resins with CQ/EDAB and NPPOC-TMG are shown in Fig. 3b. Irradiation of resins containing 0.5 wt% CQ (39.9 mol eq. vs GC2) and 1 wt% EDAB (68.8 mol eq. vs GC2) with 470 nm light at 120 mW cm<sup>-2</sup> increased front velocity (*v<sub>f</sub>*) by 12 ± 2% and by 30 ± 3% at 1 wt% CQ and 2 wt% EDAB, as calculated from the maximum value of the slope of front position versus time in the irradiated channels vs the control channels.

For the wavelength-orthogonal system, camphorquinone (CQ) and EDAB with NPPOC-TMG were selected. As the Bowman group previously reported, NPPOC-TMG has very low absorption above 420 nm and extremely slow activation upon irradiation at 455 nm<sup>49</sup>. Thus, we expected NPPOC-TMG activation at 470 nm would also be negligible. To demonstrate the orthogonality of this system, 3-channel experiments with formulations including both NPPOC-TMG and CQ/EDAB were performed. In these experiments, the front was split into three channels and irradiated with 365 nm light (left channel), unirradiated (center channel), or 470 nm light (right channel). To increase the visual contrast of the front, 0.5 wt% of a thermochromic dye with a color transition from black to clear at 35 °C was added. Upon irradiation the accelerated front propagates ahead of the unirradiated control and the inhibited front trails behind (Fig. 3c, Supplementary Movie 2).

### Photoinhibition with preirradiation

Though effective, the high intensities of light used for in situ photo-control are not always feasible to employ. Thus, we also investigated FROMP inhibition with lower intensity light using a preirradiation approach. In these experiments the irradiated region of the test channel was irradiated for varying lengths of time and then the light turned off prior to FROMP initiation.



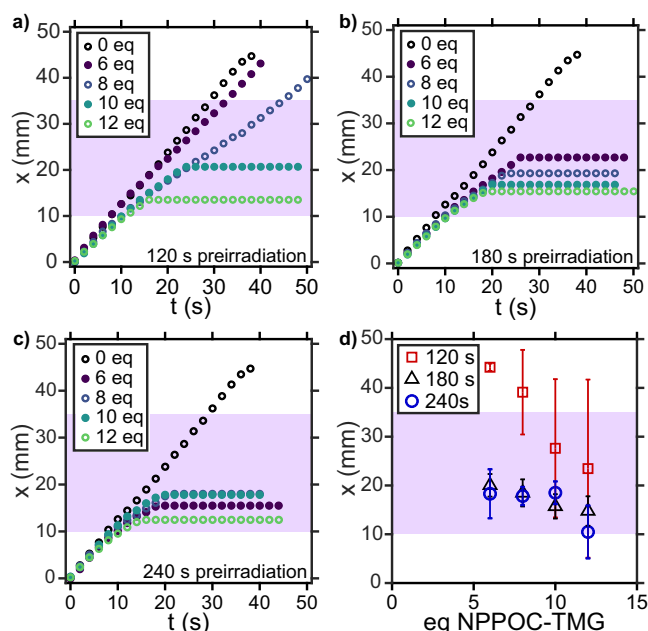


**Fig. 4 | Front inhibition with pre-irradiation.** Representative curves of front position vs time data for varying NPPOC-TMG loadings preirradiated at  $30 \text{ mW cm}^{-2}$  for (a) 120, b 180, and c 240 s. d Average  $x$ -position and standard deviation of front cessation for varying NPPOC-TMG mol eq. vs catalyst. The purple area represents the irradiated region.

We performed 2-channel experiments with preirradiation at  $30 \text{ mW cm}^{-2}$  and three different preirradiation times, with 6–12 mol eq. NPPOC-TMG (Supplementary Fig. S22, Supplementary Movie 3). Representative curves of front position versus time for each NPPOC-TMG loading and light intensity are compared and the efficacy of inhibition is quantified by the average distance the front propagates into the irradiated region (Fig. 4a–d). With 120 s of preirradiation, a correlation between inhibition and NPPOC-TMG loading was observed, although the fronts did not consistently arrest, even at higher loadings. At 180 s and 240 s of preirradiation, front cessation occurs rapidly for all formulations, nearly independent of NPPOC-TMG loading between 6 and 12 equivalents.

### Photopatterning FROMP

Typically, a FROMP front propagates radially in all directions unless blocked by a barrier, such as the wall of a mold or another propagating front<sup>24,50</sup>. Given the efficacy of the preirradiation strategy, we considered whether photobase generation could be used to create a chemical barrier to front propagation with a well-defined spatial pattern. Specifically, in which TMG photorelease inhibits FROMP in irradiated regions while the front propagates within a patterned dark region.

All patterning tests were performed using 1.3 mm thick layers of DCPD resin between two 1 mm thick glass slides and were preirradiated for 180 s with  $30 \text{ mW cm}^{-2}$  385 nm light. The resins contained 8 mol eq. NPPOC-TMG versus catalyst.

To initially quantify patterning capabilities, lines of varied widths were frontally polymerized using patterned projections (Fig. 5a, Supplementary Movie 4). Samples were preirradiated with patterned light then FROMP was initiated at the edge of the dark “T” shaped region. The widths of the horizontal bar were varied to determine the minimum line width for FROMP propagation, given the inherent instabilities of the FROMP system (Fig. 5a,b). At widths <10 mm, the fronts failed to propagate the length of the patterned region. At widths of 10 mm, front cessation still occurred in one out of three tests. We

attribute this variability to the balance between effective photo-inhibition and the volumetric requirements of front propagation. When the volume of resin available to sustain a propagating front is decreased, as in a narrower channel, the heat generated during polymerization may be insufficient to sustain the front, resulting in quenching of the front<sup>35,51</sup>. Polymerizations using projected channels with widths >10 mm were found to propagate reliably but with varying fidelity along the length of the patterned channel (Fig. 5c).

To better characterize the pattern fidelity samples with 10, 15, and 20 mm wide horizontal bars were prepared and the width of the patterned polymer ( $w_{\text{polymer}}$ ) compared to the nominal projected width ( $w_{\text{projection}}$ ) (Fig. 5a–c). Near  $x = 0$ , all patterns exhibit some overcure as the propagating front is directed from the vertical to horizontal patterned regions (Fig. 5d–f). The pattern fidelity is also poor at the far end of the channels, likely due to additional heat loss from the resin at the exposed end of the glass slides<sup>51</sup>.

These results demonstrate the sensitivities of this photopatterning strategy to multiple variables. Heat loss to the surroundings can cause the front to quench in the dark region if the total volume of the propagating front is too small. Thermal diffusion from the propagating front and polymerized material adjacent to the inhibited regions may also overcome the inhibition and result in overcuring or thermal breakout, e.g. the propagation of the front into the irradiated region. Finally, diffusion of TMG from the irradiated region into the dark region can both decrease TMG concentration in the irradiated region and increase TMG concentration in the dark region. This can contribute to breakout into irradiated regions or to unwanted arrest of the front in the dark region. Despite these limitations, this patterning approach enables a level of spatial control of front propagation that has not yet been achieved except by physical barriers.

To test the limits of this method we investigated photopatterning of more complex shapes. Arrows with a radiused  $90^\circ$  turn (Fig. 6b, Supplementary Movie 5), ‘U’s with two square  $90^\circ$  turns (Fig. 6a, Supplementary Movie 6), and “traffic islands” with rectangular and hexagonal central regions were patterned (Fig. 6c, d, Supplementary Fig. S24 and Movies 7 and 8). As in earlier experiments, patterned regions of insufficient width (<12 mm) resulted in fronts that frequently quenched (Supplementary Movie 9). The width and geometry of the central inhibited regions (Fig. 6b–d) were also found to be critical to the success of the patterning. In our system the efficacy of inhibition is highly sensitive to local temperature and therefore to the volume of inhibited resin between propagating fronts. The resin in the central regions is heated from multiple sides during FROMP patterning, thus smaller central inhibition regions, or geometries like the hexagonal “traffic island,” are more susceptible to thermal breakout and subsequent curing of the entire central region. TMG diffusion may also be an increasingly important factor as the geometries of the central irradiated region are varied.

Though the limitations on the width of the inhibition regions are very important when fronts converge, when fronts propagate parallel to each other, relatively narrow inhibition regions are possible. Dog bones with a 5.5 mm inhibited region separating the fronts at the closest points (Fig. 6e) were patterned and breakout between the propagating fronts was not observed. Finally, we demonstrated FROMP patterning with embedded objects to create multimaterial parts. A polypropylene shim was sequentially embedded into multiple FROMP-patterned regions to create a simple model wind turbine blade (Fig. 6f, Supplementary Movie S10).

In summary, our work demonstrates that front propagation in frontal ring-opening metathesis polymerization is effectively controlled through well-designed photochemistries, despite the high temperatures and rapid reaction rates of frontal polymerizations. We have shown that front velocity is controlled using catalyst-based inhibition with photobase generators or orthogonally accelerated through the addition of photosensitizers. The effects of photobase

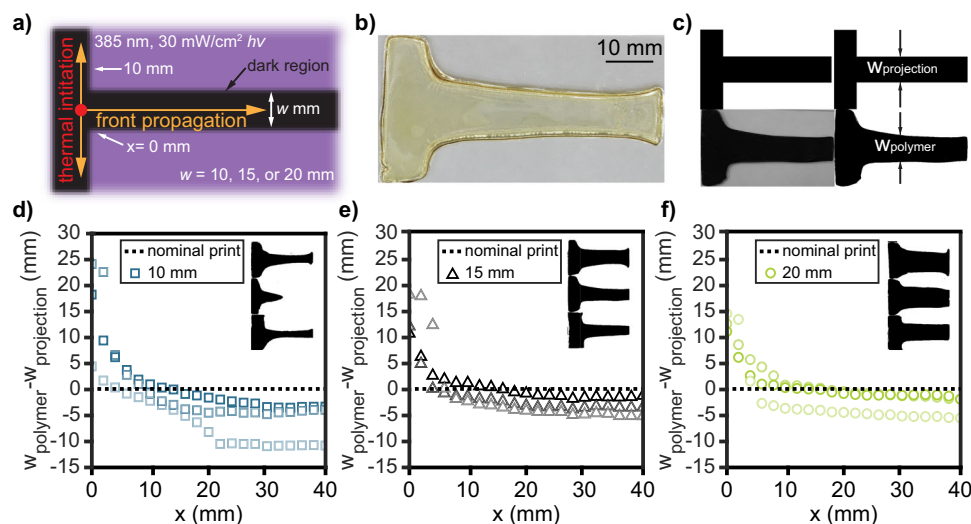


**Fig. 5 | Fidelity of frontal polymerization photoinhibition.** **a** Schematic of line width patterning experiments. **b** Image of patterned frontally polymerized pDCPD after removal of unpolymerized resin. **c** Grayscale and binarized images of patterned polymers for image analysis, and **d–f** pattern fidelity across the length of the patterned channel for different channel widths, the insets show the grayscale images of the polymerized regions for each run. To quantify the pattern fidelity the difference between the width of the patterned polymer,  $w_{\text{polymer}}$ , and that of the

projection,  $w_{\text{projection}}$ , was compared along the length of the patterned region. A perfectly patterned polymer would have  $w_{\text{polymer}} - w_{\text{projection}} = 0$  over the entire length. A value less than 0 indicates the polymerized region is narrower than the projected pattern and a value greater than 0 indicates that the polymerization front has propagated outside the patterned region (overcure). See Supplementary Movie 4 for channel experiments. See Fig. S23 for additional plots.

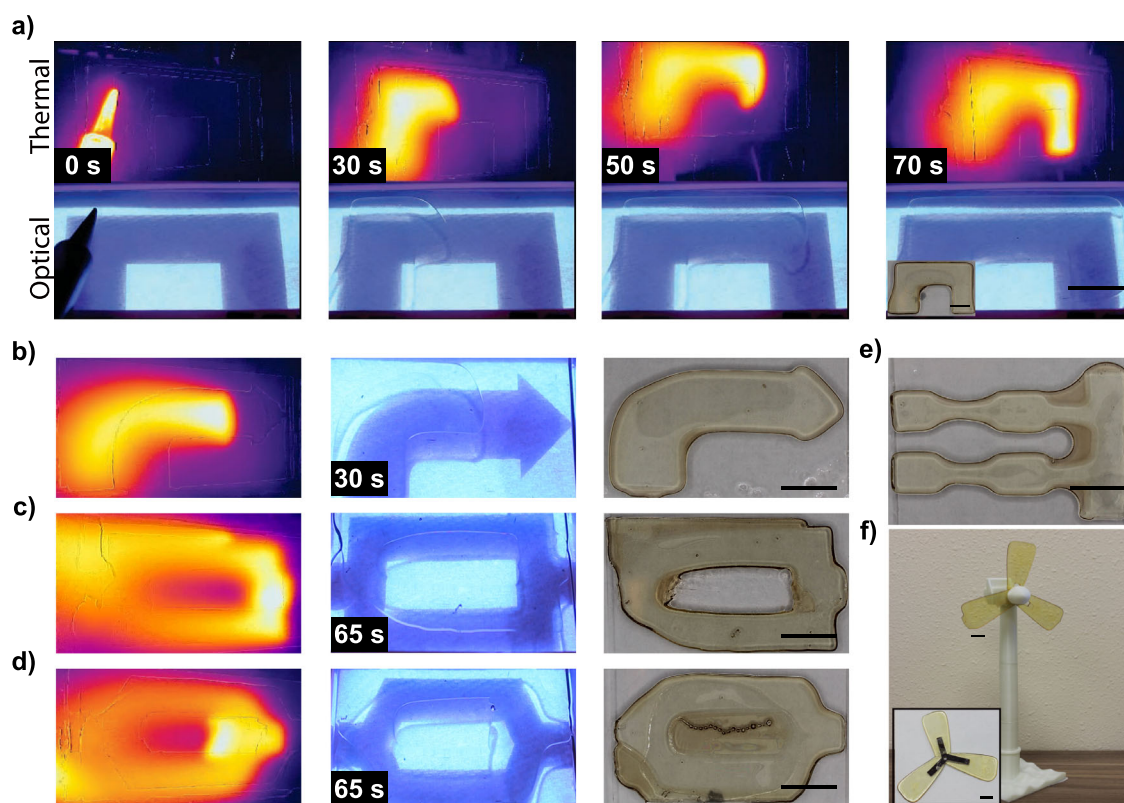


**Fig. 6 | Photopatterning FROMP.** Projections and resulting patterned polymers for **(a)** a square “U” with 180° front redirection **(b)** a 90° radiused arrow and traffic island patterns with **(c)** a rectangular island and **(d)** an elongated hexagonal island, showing how geometry can impact inhibition and breakout. Thermal images for the sample with the hexagonal island show FROMP back propagation through the

inhibited area when the parallel propagating fronts converge, whereas with the square inhibition area breakout into the central region does not occur when the fronts converge. FROMP photopatterned **(e)** tensile bars and **(f)** turbine blades with embedded struts are also presented. Scale bars are 10 mm.

generator loading, light intensity, and irradiation dose were examined, and a resin system was developed for photopatterning of FROMP polymers. Using photopatterning, we demonstrated directional control of front propagation to generate predefined geometries and features such as 180° turns, “punch-out” dogbones, and patterned overmolding. We anticipate that this system can be used in DIW additive manufacturing with FROMP for in situ control of the front velocity and in morphogenic manufacturing<sup>36,37</sup> to introduce active spatial control of front propagation and spin modes. Moreover, we hope this system will inspire the development of analogous photo-control chemistries for other frontal polymerization systems. Future investigations will seek to better understand the mechanism of catalyst-based inhibition and the contributions of thermal and chemical diffusion to front propagation and pattern fidelity.

## Methods

### Materials

All DCPD resins in this work contain 5 wt% 5-ethylidene-2-norbornene to lower the melting point so that they are liquids at room temperature.

Dicyclopentadiene (DCPD, ULTRENE, 97%) was obtained from Cymetech. Tributyl phosphite (TBP, 93%), 5-ethylidene-2-norbornene (ENB, 98%), 2-(2-nitrophenyl)propanol (98%) and ethyl 4-(dimethylamino)benzoate (EDAB, >98%) were obtained from TCI. Grubbs' second generation catalyst (1,3-bis(2,4,6-trimethylphenyl)-2-imidazolidinylidene)dichloro (phenylmethylene) (tricyclohexylphosphine)ruthenium (GC2, CAS 246047-72-3), dichloromethane (DCM, 99.8%), 1,2-dichloroethane (DCE, ≥99%), 1,1,3,3-tetramethylguanidine (TMG, 99%), carbonyl diimidazole (CDI, 96–98%) camphorquinone (CQ, 97%) and tetracyclohexylphosphonium chloride (≥95%) were purchased from Sigma Aldrich. 2-(2-nitrophenyl)propyl carbonochloridate (95%) was purchased from Aaron Chemicals. Benzophenone (98%), 2-isopropylthioxanthone (ITX, 98%), and 1,2-diphenylethane-1,2-dione (benzil) (98%) were purchased from aaBlocks. Methanol (MeOH, 99.9%) and sodium hydroxide (NaOH >97%) were purchased from Fischer Scientific. Thermochromic pigment (black/clear 95 °F/35 °C) was purchased from Atlantic Chemical. Phenolsulfonphthalein (phenol red) was purchased from Matheson Coleman & Bell. Sodium sulfate (Na<sub>2</sub>SO<sub>4</sub>, 99.5%), CD<sub>2</sub>Cl<sub>2</sub> (99.8%) and DMSO-d<sub>6</sub> (>99.8%) were purchased from Oakwood Chemical. Chloroform-d (CDCl<sub>3</sub>, 99.8%) was purchased from Cambridge Isotope Laboratories. All commercial chemicals were used without further purification. Silicone molds were made using RTV-630 silicone rubber molding compound (Momentive).

### 2-(2-Nitrophenyl)propyl-N-(1,1,3,3-tetramethylguanidiny)carbamate (NPPOC-TMG) Synthesis

NPPOC-TMG was synthesized by two methods depending on the most readily available starting material. Note: Due to the light sensitivity of NPPOC-TMG if autocolumns are used the UV detector should be turned off.

Route 1: Starting with 2-(2-nitrophenyl)propanol a modified method similar to that reported in Foster, et al<sup>33</sup>, was used. 2-(2-Nitrophenyl)propanol (3.50 g, 14.32 mmol, 1 mol eq.) is loaded into a 150-mL round-bottom flask equipped with a magnetic stir bar. DCM (55 mL) is added, followed by carbonyl diimidazole, portion-wise (4.85 g, 29.94 mmol, 1.55 mol eq.). The reaction is capped with a septum vented with a needle, covered in aluminum foil to prevent light from entering, and stirred at room temperature for 4 hours. 1,1,3,3-Tetramethylguanidine (9.94 mL, 79.20 mmol, 4.1 mol eq.) is then added slowly and the reaction is stirred at room temperature overnight for ~18 hours. The reaction is quenched with water (30 mL) and extracted with DCM (20 mL). The organic extracts are combined, washed with water (3 × 15 mL), brine (20 mL), and dried over anhydrous Na<sub>2</sub>SO<sub>4</sub>. The solvent is removed in a rotary evaporator at 60 °C and the crude product is purified using column chromatography (SiO<sub>2</sub>, 20% MeOH/DCM, liquid-loading), resulting in NPPOC-TMG as a dark red-

orange oil that crystallized under high vacuum (< 50 mTorr). Yield: 5.23 g, 84%.

Route 2: 2-(2-nitrophenyl)propyl carbonochloridate (5.0 g, 20.52 mmol, 1 mol eq.) is loaded into a 500-mL round-bottom flask equipped with a magnetic stir bar. Dichloromethane (160 mL) is added and cooled to 0 °C. 1,1,3,3-Tetramethylguanidine (5.15 mL, 41.04 mmol, 2 mol eq.) is added dropwise to the reaction mixture, which is then capped with a septum vented with a needle, covered in aluminum foil to prevent light from entering, and allowed to warm to room temperature overnight for a period of ~18 hours. The reaction is quenched with water (50 mL) and extracted with dichloromethane (30 mL). The organic extracts are combined, washed with water (3 × 25 mL), brine (30 mL), and dried over anhydrous Na<sub>2</sub>SO<sub>4</sub>. The solvent is removed in a rotary evaporator at 60 °C and the crude product is purified using column chromatography (SiO<sub>2</sub>, 20% MeOH/DCM, liquid-loading), resulting in NPPOC-TMG as a brown-orange oil that crystallized under high vacuum (< 50 mTorr). Yield: 5.08 g, 77%.

<sup>1</sup>H NMR (500 MHz, CDCl<sub>3</sub>, SI Figure S5): δ (ppm) 7.72 (d, 1H), 7.53 (m, 2H), 7.30 (td, 1H), 4.27 (d, 2H), 3.69 (m, 1H), 2.80 (s, 12H), 1.36 (d, 3H).

### Resin formulations

**Monomer stock formulation.** A mixture of 95:5 (wt:wt) of DCPD and ENB is prepared by adding melted DCPD (40–50 °C) to a jar with ENB and mixing.

**FROMP stock formulation.** Tributyl phosphite (TBP, 2.85 μL) is added to a 20-mL vial then diluted with monomer stock mixture (15 g) to reach 100 ppm TBP. Mixtures are used within 1 hour to minimize effects of TBP evaporation. GC2 is added to a 20-mL vial (9.6 mg) and dissolved with stock TBP inhibited resin (15 g). The resin is then sonicated for 5 minutes to dissolve GC2. After the addition of GC2 resins should be used within 1 h.

**Photocontrol resin formulation.** Photocontrol resins are prepared by massing all additives (photobase generator, photosensitizers) into 20-mL glass vials, dissolving in DCM (12 μL/g of total resin), and adding FROMP stock formulation to reach the target NPPOC-TMG or photosensitizer loading. Nominal values for a 15 g DCPD resin formulation are included in Supplementary Table S5. Resins shown in the text with 0 molar equivalents of NPPOC-TMG to catalyst or 0 wt% photosensitizer are still mixed with 12 μL DCM/g resin to ensure consistency with the active formulations.

**Resins with TMG.** Resins with known quantities of TMG are prepared by diluting 6.6 μL TMG in 7 g of FROMP resin to yield a 10 mol eq. TMG: GC2 solution. This stock is then diluted with standard FROMP resin to 8, 6, 4, and 2 mol eq. TMG: GC2. See discussion for Supplementary Fig. S13 for additional details of the testing of resins with direct addition of TMG.

### Light sources

Exposures with 365 nm light use a Dymax Qx4 LED. Patterning experiments were performed at 385 nm with a Titan projector (PRO6500). Exposures with 470 nm light use a ThorLabs M470LS-CL LED. Irradiation intensity is measured using a TA Silverline radiometer for 365 and 385 nm light or a ThorLabs PM100D radiometer with an S120VC sensor for 470 nm light.

### 2- and 3-channel tests

Front velocity is highly dependent on catalyst and phosphite inhibitor concentration and significantly varies batch-to-batch due to small variations in the resin formulation. Multichannel tests were used to enable measurement of control and irradiated channels with resin from the same batch, with fronts initiated at the same time. In the multichannel tests, silicone molds were filled with a single batch of



resin, covered with a 1 mm thick glass cover slide, and a front was initiated at the top of the mold. The mold geometry (Supplementary Fig. S3) splits the propagating front into multiple channels so that the front velocities of the unirradiated control channel and the irradiated test channel can be directly compared (Supplementary Movies 1 and 2). Previous work has shown that, at resin depths thinner than 1.25 mm, FROMP becomes unstable<sup>31</sup>, thus, the channels were made 1.3 mm deep to ensure optimal light penetration while maintaining a sufficient volume of resin to sustain front propagation. Photographs of the molds, and images and stl files of the negatives are included (Supplementary Fig. S3, Supplementary Dataset 1).

**2-channel tests.** Two channel tests were used for quantification of inhibition and acceleration. Silicone molds with channels (45 mm×10 mm x 1.3 mm) and an initiation area at the top were prepared (Figs. 1, 3c, Supplementary Fig. S3). The initiation region splits the propagating front into 2 channels and directs front propagation so that the fronts enter the channels at the same time. The molds are covered with 1 mm thick glass slides secured with binder clips. The mold is arranged vertically and then loaded with resin.

Samples were irradiated using a Dymax QX4 with a Redicure attachment and an 8 mm lens. The lens was positioned 3.5 cm away from the sample, and a radiometer was used to create a source power vs light intensity standard curve at the beginning of each experiment session. The irradiation pattern was a 25 mm×25 mm square positioned to cover one channel from  $x = 10$  to 35 mm. During in situ irradiation testing the light was turned on when the front crossed the  $x = 10$  mm hash mark. During preirradiation tests, the internal timer on the QX4 was used to control preirradiation time at a fixed intensity and FROMP was initiated as the light turned off.

FROMP is initiated by holding a Weller soldering iron heated to 450 °C against the glass slide near the top of the resin in the mold until FROMP begins. For 2-channel experiments one channel is a control (unirradiated) and one channel is irradiated. Tests with thermo-chromic dye were not used for front velocity quantification. Tracker (version 6.1.6, open source, <https://physlets.org/tracker/>) is used to monitor the front positions versus time in 2-channel tests.

**3-channel tests.** Three-channel tests were performed only for qualitative demonstration of orthogonal inhibition/acceleration, quantitative measurements of the inhibition and acceleration of front velocity were made with two-channel tests. Silicone molds with three channels (45 mm×10 mm x 1.3 mm) and an initiation area at top were prepared (Figs. 1, 3c, and Supplementary Fig. S3). The initiation region splits the propagating front into 3 channels and directs front propagation so that the fronts enter all three channels at the same time. The molds are filled with resin and the front initiated in the same manner as described for the 2-channel tests. For the three-channel experiments the center channel is the control and the right (365 nm, inhibition) and left (470 nm, acceleration) channels are irradiated with different wavelengths of light. Both channels were irradiated for 30 s of preirradiation and then irradiated continuously in a zone from 10 to 30 mm during FROMP propagation. For some of these tests 0.5 wt% thermo-chromic dye (black/clear 35 °C, Atlantic Chemical) is incorporated into the resin to improve the visualization of the front.

### Patterning experiments

Patterning samples were prepared using a standard FROMP resin with 8 mol eq. NPOC-TMG versus catalyst. Shims (2 stacked shims, 60 mm×5 mm x 0.635 mm) were clamped between glass slides (45 mm×70 mm x 1 mm). Resin was carefully pipetted between slides to form a 1.3 mm thick layer. A Titan projector (PRO6500, 385 nm) on a support stand projects images onto the resin filled glass slides at 385 nm and 30 mW cm<sup>-2</sup> with preirradiation times as specified for each experiment. The projector was focused with a biconvex lens (Ø2";

$f = 100$  mm; NA, 0.76; Thorlabs, LB1630). FROMP was initiated with a Weller soldering iron heated to 450 °C and held against the glass until FROMP begins. Front progression and patterning fidelity images and video were recorded. Thermal videos were taken with a FLIR One thermal camera. The maximum light intensity in these experiments is limited by the light engine used to project the patterned images.

**Patterning — channel width image analysis.** Glass slides were prepared as described above without resin. Paper was clamped to the top, and the projected pattern was traced and used to define the projection region. After patterning, unreacted resin was washed away and the polymerized pDCPD samples were darkened with a black marker. Digital photographs were taken before and after darkening. The images of the darkened samples were then cropped to a standard size for analysis. A custom MATLAB code resized images, converted to grayscale, and binarized. The width of the projection and pattern were determined by summing the pixel count at regular x-axis intervals (100 pixels = 1 mm). Nominal projection widths are subtracted from the widths of the patterned polymer to determine the pattern fidelity.

### Differential scanning calorimetry (DSC)

All DSC measurements were conducted on a TA instruments Discovery X3 differential scanning calorimeter in sealed aluminum hermetic pans. All DSC plots are presented as “exo up.” Cure kinetics tests are conducted by loading 2 µL of resin into a pan, sealing, then loading into an autosampler. Samples are run immediately after loading or kept in a -20 °C freezer until they can be run. The DSC procedure is: cool to 0 °C, 1-minute isotherm, cool to -20 °C at 20 °C/min, 5-minute isotherm, heat to 250 °C at 7 °C/min. The exotherm resulting from polymerization is measured by integrating the normalized heat flow from 45 to 160 °C. For DSC on polymerized samples, samples are cut into small pieces and are loaded into pans at -10 mg/pan and analyzed with a heat-cool-heat process from 0 °C to 250 °C at 10 °C/min. NPOC-TMG is analyzed using the same parameters.

### TGA

Thermogravimetric analysis was performed on a TA instruments Q5500 thermogravimetric analyzer. Samples are heated at 10 °C/min under nitrogen from 25 °C to 300 °C in platinum pans.

### DMA

Dynamic mechanical analysis was conducted on an ARES-G2 rheometer (TA Instruments) at 1 Hz and 1% strain. Variable temperature tests are run from 50 °C to 250 °C at 3 °C/min. Samples are 9 mm wide by 2 mm thick by -15 mm long.

### NMR

Nuclear magnetic resonance spectra were recorded using a Bruker AVANCE III 500 spectrometer with chloroform-d ( $\text{CDCl}_3$ ) or dichloromethane-d<sub>2</sub> ( $\text{CD}_2\text{Cl}_2$ ) as a solvent. Shifts are reported in parts per million (ppm) relative to solvent residual peak (7.26 ppm,  $\text{CDCl}_3$ ; 5.32 ppm  $\text{CD}_2\text{Cl}_2$ ).

### UV-Vis

UV-Vis experiments were performed on an Agilent Cary 60 UV-Vis. Samples were measured either in 1 cm or 0.1 cm path length quartz cuvettes as indicated for specific experiments. Spectra were acquired from 200 to 800 nm with an averaging time of 0.0125 s, a data interval of 1 nm, and a scan rate of 4800 nm/min.

### NPOC-TMG activation experiments: NMR

A 1:100 NPOC-TMG:DCPD/ENB mixture was prepared by dissolving 50 mg of NPOC-TMG (0.16 mmol) in minimal DCM and then combining with 2 g of DCPD/ENB (15.2 mmol). This solution was then pipetted into 1×1 cm wells of varying depth (0.5–1.5 mm) and irradiated



with 365 nm light ( $30 \text{ mW cm}^{-2}$  or  $180 \text{ mW cm}^{-2}$ ) or 385 nm light ( $30 \text{ mW cm}^{-2}$ ) for varying times up to 300 s. After irradiation 25  $\mu\text{L}$  of the mixture in each well was then dissolved in 600  $\mu\text{L}$  of  $\text{CD}_2\text{Cl}_2$  and the NMR spectrum of each was collected. The DCPD/ENB peaks at 5.98 (d, 1H) and 5.52 (d, 1H) ppm are normalized to 1, then the NPPOC-TMG (starting material) peaks at 7.75 (d, 1H), 7.60 (m, 2H), and 7.39 (td, 1H) ppm are integrated and the average 1H integration value is used to calculate NPPOC-TMG activation, relative to the initial (unirradiated) concentration. Note that the NPPOC-TMG peaks at 7.60 and 7.39 ppm overlap with a 1H peaks of the nitrostyrenyl byproduct of NPPOC-TMG degradation. The integration values must be corrected by subtracting the byproduct peak value estimated by using the integrated values for the byproduct peaks at 7.89 (dd, 1H) and 7.46 (td, 1H) ppm to obtain accurate integration values for the NPPOC-TMG peaks.

#### NPPOC-TMG activation experiments: UV-Vis in dichloroethane

Samples were measured in quartz cuvettes with a 1 cm path length.

A 1 mM solution of phenol red pH indicator was prepared by dissolving 88.5 mg of phenol red in 250 mL of dichloroethane (DCE). Calibration controls with varying TMG concentrations (1.74 mg, 3.47 mg, 5.21 mg, 6.94 mg, and 8.68 mg) were prepared in 10 g of DCE, corresponding to the TMG concentrations generated for a nominally 100% efficient activation of 2, 4, 6, 8, and 10 mol eq. of NPPOC-TMG relative to the catalyst in the standard resin formulation. A volume of 100  $\mu\text{L}$  of TMG solution was added to 300  $\mu\text{L}$  of the indicator solution and 800  $\mu\text{L}$  of DCE. The absorbance values of these controls were used to generate a calibration curve for TMG concentration.

The activation of NPPOC-TMG was then measured by irradiating a dichloroethane solution matching the GC2 and NPPOC-TMG concentrations in a resin with 8 mol eq. NPPOC-TMG:GC2. A solution was prepared by dissolving 6.4 mg of GC2 and 19.5 mg of NPPOC-TMG in 10 g of DCE. DCE was chosen over DCPD to prevent background curing during light exposure and to limit solvent evaporation. Activation rates were measured in 1.3 mm-deep wells at  $30 \text{ mW/cm}^2$  (385 nm), which corresponds to the intensity and wavelength used for photopatterning, as well as at  $180 \text{ mW/cm}^2$  (365 nm), the intermediate intensity employed in 2-channel front inhibition experiments. Test solutions were pipetted into the wells and irradiated for varying times up to 300 seconds. After irradiation, aliquots of the solutions (100  $\mu\text{L}$ ) were collected, mixed with 300  $\mu\text{L}$  of the indicator solution, and diluted with 800  $\mu\text{L}$  of DCE to match the preparation of the calibration samples. The UV-Vis spectra were then measured. Photobase generation was assessed by comparing the phenol red absorption peak intensity at 570 nm in the irradiated samples to the calibration standards to calculate the concentration of released TMG. All irradiation conditions and concentrations were tested in duplicate, and the results were averaged.

#### NPPOC-TMG activation experiments: UV-Vis in DCPD

Samples were measured in quartz cuvettes with a 0.1 cm path length.

**Indicator solution.** A 0.0072 M solution of ionic liquid phenol red indicator was prepared by dissolving 80.8 mg of the ionic liquid phenol red in 8.5 mL of DCPD.

**Calibration curve.** Calibration controls with varying TMG amounts (1.74 mg, 3.47 mg, 5.21 mg, 6.94 mg, and 8.68 mg) were prepared in 10 g of DCPD, corresponding to the TMG concentration generated for a nominally 100% efficient activation of 2, 4, 6, 8, and 10 mol eq. of NPPOC-TMG relative to the catalyst in the standard resin formulation. A volume of 100  $\mu\text{L}$  of the TMG standard solutions was added to 350  $\mu\text{L}$  of the indicator solution and diluted with 600  $\mu\text{L}$  of DCPD, and 100  $\mu\text{L}$  of DCM. The resulting absorbance values of these controls were used to generate a calibration curve for comparison to NPPOC-TMG containing samples after irradiation.

The activation of NPPOC-TMG was then measured by irradiating a solution matching the NPPOC-TMG concentration of an 8 mol eq. resin. GC2 was omitted from the resin to eliminate background curing of the DCPD containing samples. A solution was prepared by dissolving 19.5 mg of NPPOC-TMG in 10 g of DCPD. Activation rates were measured in 1.3 mm-deep wells at  $180 \text{ mW/cm}^2$  (365 nm), the intermediate intensity employed in 2-channel front inhibition experiments. Test solutions were pipetted into the wells and irradiated for varying times up to 240 seconds. After irradiation, aliquots of the solutions (100  $\mu\text{L}$ ) were mixed with 350  $\mu\text{L}$  of the indicator solution, and diluted with 600  $\mu\text{L}$  of DCPD and 100  $\mu\text{L}$  of DCM to match the preparation of the calibration samples. The UV-Vis spectra were then measured. Photobase generation was assessed by comparing the ionic liquid maximum absorption peak intensity between 550 and 600 nm in the irradiated samples to the calibration standards to calculate the concentration of released TMG.

#### Phenol red sodium salt synthesis

This procedure is adapted from Pramanik et al.<sup>52</sup>. Phenol red (700 mg, 1.98 mmol, 1 eq) is dispersed in MeOH (100 mL). Separately, NaOH (79 mg, 1.98 mmol, 1 eq) is dissolved in MeOH (100 mL), then added to phenol red solution. The reaction is stirred for 4 hours at room temperature. The solvent is removed in a rotary evaporator at  $60^\circ\text{C}$ , resulting in a dark red solid, which is used in the following step without further purification. Yield: 715 mg (96%).

#### Phenol red ionic liquid synthesis

This procedure is adapted from Pramanik et al.<sup>53</sup>. Phenol red sodium salt (500 mg, 1.33 mmol, 1 eq) is dissolved in water (45 mL). Separately, tetradecyltriethylphosphonium chloride (1.38 g, 2.66 mmol, 2 eq) is dissolved in DCM (90 mL), then added to phenol red sodium salt solution. The reaction is capped with a septum equipped with a vent needle and stirred at room temperature for 17 hours. The reaction is quenched with water (50 mL) and extracted with DCM (50 mL). The organic extracts are combined, washed with water ( $3 \times 500 \text{ mL}$ ), and dried over anhydrous  $\text{Na}_2\text{SO}_4$ . The solvent is removed in a rotary evaporator at  $60^\circ\text{C}$ , resulting in the phenol red ionic liquid as a dark red, viscous oil (composition = 1:2 phenol red:  $\text{P}_{6,6,6,14}\text{Cl}$ ). Yield: 1.61 g (92%).  $^1\text{H}$  NMR (500 MHz,  $\text{DMSO}-d_6$ ,  $25^\circ\text{C}$ ):  $\delta$  (ppm) 10.04 (br s, 1H), 7.89 (d, 1H), 7.40 (t, 1H), 7.35 (t, 1H), 7.30–7.01 (br m, 4H), 6.93 (d, 1H), 6.71–6.34 (br m, 4H), 2.21–2.14 (m, 16H), 1.49–1.42 (m, 16H), 1.39–1.34 (m, 16H), 1.31–1.26 (m, 32H), 1.24 (s, 32H), 0.89–0.84 (m, 24H).

#### Nitrostyrene fragment isolation/purification

NPPOC-TMG (500 mg, 1.55 mmol) is dissolved in DCM (10 mL) and the solution is placed into a crystallization dish ( $60 \times 15 \text{ mm}$ ) with a stir bar, then irradiated with 365 nm light (Dymax BlueWave AX-550) at  $130 \text{ mW/cm}^2$  intensity for 5 min while stirring. The resultant mixture is extracted with DCM (50 mL) and washed with water ( $3 \times 250 \text{ mL}$ ), brine (100 mL), and dried over anhydrous  $\text{Na}_2\text{SO}_4$ . The solvent is removed in a rotary evaporator at  $60^\circ\text{C}$  and the crude product is purified with column chromatography ( $\text{SiO}_2$ , solid-loading) using a gradient elution from 0 to 100% DCM/hexanes over 5 minutes, resulting in the nitrostyrene fragment as a light brown oil. Yield: 90 mg, 35.6%.  $^1\text{H}$  NMR (500 MHz,  $\text{CD}_2\text{Cl}_2$ ,  $25^\circ\text{C}$ ):  $\delta$  (ppm) 7.84 (dd, 1H,  $\text{CH}_{\text{Ar}}$ ), 7.57 (dt, 1H,  $\text{CH}_{\text{Ar}}$ ), 7.42 (dt, 1H,  $\text{CH}_{\text{Ar}}$ ), 7.35 (dd, 1H,  $\text{CH}_{\text{Ar}}$ ), 5.17 (t, 1H,  $\text{C}=\text{CH}_2$ ), 4.93 (s, 1H,  $\text{C}=\text{CH}_2$ ), 2.08 (s, 3H,  $\text{C}-\text{CH}_3$ ).

#### Data availability

The data that supports the findings of this study are available within the paper and its supplementary information files. Supplementary data files are identified by Figure or SI Figure numbers. All data are available from the corresponding author upon request. Source data are provided with this paper.

## References

- Mariani, A., Fiori, S., Chekanov, Y. & Pojman, J. A. Frontal ring-opening metathesis polymerization of dicyclopentadiene. *Macromolecules* **34**, 6539–6541 (2001).
- Ruiu, A., Sanna, D., Alzari, V., Nuvoli, D. & Mariani, A. Advances in the frontal ring opening metathesis polymerization of dicyclopentadiene. *J. Polym. Sci. Part A: Polym. Chem.* **52**, 2776–2780 (2014).
- Robertson, I. D. et al. Rapid energy-efficient manufacturing of polymers and composites via frontal polymerization. *Nature* **557**, 223–227 (2018).
- Suslick, B. A. et al. Frontal polymerizations: from chemical perspectives to macroscopic properties and applications. *Chem. Rev.* **123**, 3237–3298 (2023).
- Xu, Z. C. et al. Reactive processing of Furan-based monomers via frontal ring-opening metathesis polymerization for high performance materials. *Adv. Mater.* <https://doi.org/10.1002/adma.202405736> (2024).
- Goli, E. et al. Frontal polymerization accelerated by continuous conductive elements. *J. Appl. Polym. Sci.* <https://doi.org/10.1002/app.47418> (2019).
- Tran, A. D., Koch, T., Knaack, P., & Liska, R. Radical induced cationic frontal polymerization for preparation of epoxy composites. *Compos. Part A-Appl. Sci. Manufact.* <https://doi.org/10.1016/j.compositesa.2020.105855> (2020).
- Ziaee, M., Johnson, J. W. & Yourdkhani, M. 3D printing of short-carbon-fiber-reinforced thermoset polymer composites via frontal polymerization. *ACS Appl. Mater. Interfaces* **14**, 16694–16702 (2022).
- Hmeidat, N. S. et al. Reactive extrusion of frontally polymerizing continuous carbon fiber reinforced polymer composites. *Compos. Part A-Appl. Sci. Manufact.* <https://doi.org/10.1016/j.compositesa.2024.108609> (2025).
- Chen, S., Sui, J., Chen, L. & Pojman, J. A. Polyurethane-nanosilica hybrid nanocomposites synthesized by frontal polymerization. *J. Polym. Sci. Part A: Polym. Chem.* **43**, 1670–1680 (2005).
- Sanna, R. et al. Polymer hydrogels of 2-hydroxyethyl acrylate and acrylic acid obtained by frontal polymerization. *J. Polym. Sci. Part A: Polym. Chem.* **50**, 1515–1520 (2012).
- Sun, J., Zhou, L., Han, P. & Qiao, G. UV-initiated frontal polymerization for the fast synthesis of bubble-free, self-propagating hydrogel anticorrosive coatings. *ACS Appl. Mater. Interfaces* **15**, 28618–28625 (2023).
- Yan, Q. Z., Zhang, W. F., Lu, G. D., Su, X. T. & Ge, C. C. Frontal polymerization synthesis of starch-grafted hydrogels: Effect of temperature and tube size on propagating front and properties of hydrogels. *Chem.-A Eur. J.* **12**, 3303–3309 (2006).
- Chekanov, Y. A. & Pojman, J. A. Preparation of functionally gradient materials via frontal polymerization. *J. Appl. Polym. Sci.* **78**, 2398–2404 (2000).
- Nuvoli, D. et al. Synthesis and characterization of functionally gradient materials obtained by frontal polymerization. *ACS Appl. Mater. Interfaces* **7**, 3600–3606 (2015).
- Bistri, D. et al. A mechanism-based reaction-diffusion model for accelerated discovery of thermoset resins frontally polymerized by olefin metathesis. *J. Am. Chem. Soc.* **146**, 21877–21888 (2024).
- Aw, J. E. et al. Self-regulative direct ink writing of frontally polymerizing thermoset polymers. *Adv. Mater. Technol.* <https://doi.org/10.1002/admt.202200230> (2022).
- Lessard, J. J. et al. Unraveling reactivity differences: room-temperature ring-opening metathesis polymerization (ROMP) versus frontal ROMP. *J. Am. Chem. Soc.* **146**, 7216–7221 (2024).
- McFadden, T. P. et al. Using data science tools to reveal and understand subtle relationships of inhibitor structure in frontal ring-opening metathesis polymerization. *J. Am. Chem. Soc.* **146**, 16375–16380 (2024).
- Gao, Y. et al. Manipulating frontal polymerization and instabilities with phase-changing microparticles. *J. Phys. Chem. B* **125**, 7537–7545 (2021).
- Davydovich, O. et al. Frontal polymerization of dihydrofuran comonomer facilitates thermoset deconstruction. *Chem. Mater.* **34**, 8790–8797 (2022).
- Stawiasz, K. J., Paul, J. E., Schwarz, K. J., Sottos, N. R. & Moore, J. S. Photoexcitation of Grubbs' second-generation catalyst initiates frontal ring-opening metathesis polymerization. *ACS Macro Lett.* **9**, 1563–1568 (2020).
- Stawiasz, K. J., Wendell, C. I., Suslick, B. A. & Moore, J. S. Photoredox-initiated frontal ring-opening metathesis polymerization. *ACS Macro Lett.* **11**, 780–784 (2022).
- Cook, A. L. et al. Polymer patterning by laser-induced multipoint initiation of frontal polymerization. *ACS Appl. Mater. Interfaces* **16**, 17973–17980 (2024).
- Petko, F., Swiezy, A. & Ortyl, J. Photoinitiating systems and kinetics of frontal photopolymerization processes - the prospects for efficient preparation of composites and thick 3D structures. *Polym. Chem.* **12**, 4593–4612 (2021).
- Sutar, R. L. et al. A light-activated olefin metathesis catalyst equipped with a chromatic orthogonal self-destruct function. *Angew. Chem.-Int. Ed.* **55**, 764–767 (2016).
- Teator, A. J., Shao, H. L., Lu, G., Liu, P. & Bielawski, C. W. A photo-switchable olefin metathesis catalyst. *Organometallics* **36**, 490–497 (2017).
- Eivgi, O., Vaisman, A., Nechmad, N. B., Baranov, M. & Lemcoff, N. G. Latent ruthenium benzylidene phosphite complexes for visible-light-induced olefin metathesis. *ACS Catal.* **10**, 2033–2038 (2020).
- Park, S. et al. Reversibly photoswitchable catalysts for olefin metathesis reactions. *ACS Catal.* **11**, 13860–13865 (2021).
- Greenlee, A. J., Weitekamp, R. A., Foster, J. C. & Leguizamón, S. C. PhotoROMP: The future is bright. *ACS Catal.* **14**, 6217–6227 (2024).
- Leguizamón, S. C., Cook, A. W. & Appelhans, L. N. Employing photosensitizers for rapid olefin metathesis additive manufacturing of poly(dicyclopentadiene). *Chem. Mater.* **33**, 9677–9689 (2021).
- Leguizamón, S. C. et al. Photoinitiated olefin metathesis and stereolithographic printing of polydicyclopentadiene. *Macromolecules* **55**, 8273–8282 (2022).
- Foster, J. C. et al. Continuous additive manufacturing using olefin metathesis. *Adv. Sci.* **9**, e2200770 (2022).
- Suslick, B. A., Stawiasz, K. J., Paul, J. E., Sottos, N. R. & Moore, J. S. Survey of catalysts for frontal ring-opening metathesis polymerization. *Macromolecules* **54**, 5117–5123 (2021).
- Goli, E., Gai, T. & Geubelle, P. H. Impact of boundary heat losses on frontal polymerization. *J. Phys. Chem. B* **124**, 6404–6411 (2020).
- Paul, J. E. et al. Controlled patterning of crystalline domains by frontal polymerization. *Nature* **634**, 85–90 (2024).
- Kim, Y. S. et al. Morphogenic growth 3D printing. *Adv. Mater.* **37**, 2406265 (2025).
- Compain, P. Olefin metathesis of amine-containing systems: Beyond the current consensus. *Adv. Synth. Catal.* **349**, 1829–1846 (2007).
- P'Pool, S. J. & Schanz, H. J. Reversible inhibition/activation of olefin metathesis: A kinetic investigation of ROMP and RCM reactions with Grubbs' catalyst. *J. Am. Chem. Soc.* **129**, 14200–14212 (2007).
- Wilson, G. O. et al. Stability of second generation grubbs' alkylidenes to primary amines: formation of novel ruthenium-amine complexes. *Adv. Synth. Catal.* **351**, 1817–1825 (2009).
- Manzini, S. et al. Insights into the decomposition of olefin metathesis precatalysts. *Angew. Chem.-Int. Ed.* **53**, 8995–8999 (2014).
- Maughon, B. R. & Grubbs, R. H. Ruthenium alkylidene initiated living ring-opening metathesis polymerization (ROMP) of 3-substituted cyclobutenes. *Macromolecules* **30**, 3459–3469 (1997).

43. Cormier, S. K. & Fogg, D. E. Probing catalyst degradation in metathesis of internal olefins: expanding access to amine-tagged ROMP polymers. *ACS Catal.* **13**, 11834–11840 (2023).
44. Lummiss, J. A. M., Ireland, B. J., Sommers, J. M. & Fogg, D. E. Amine-mediated degradation in olefin metathesis reactions that employ the second-generation grubbs catalyst. *ChemCatChem* **6**, 459–463 (2014).
45. Ireland, B. J., Dobigny, B. T. & Fogg, D. E. Decomposition of a phosphine-free metathesis catalyst by amines and other bronsted bases: metallacyclobutane deprotonation as a major deactivation pathway. *ACS Catal.* **5**, 4690–4698 (2015).
46. Nascimento, D. L., Reim, I., Foscatto, M., Jensen, V. R. & Fogg, D. E. Challenging metathesis catalysts with nucleophiles and bronsted base: examining the stability of state-of-the-art ruthenium carbene catalysts to attack by amines. *ACS Catal.* **10**, 11623–11633 (2020).
47. Xi, W. et al. Spatial and temporal control of thiol-michael addition via photocaged superbase in photopatterning and two-stage polymer networks formation. *Macromolecules* **47**, 6159–6165 (2014).
48. Robertson, I. D. et al. Alkyl phosphite inhibitors for frontal ring-opening metathesis polymerization greatly increase pot life. *ACS Macro Lett.* **6**, 609–612 (2017).
49. Zhang, X. et al. o-nitrobenzyl-based photobase generators: efficient photoinitiators for visible-light induced thiol-michael addition photopolymerization. *ACS Macro Lett.* **7**, 852–857 (2018).
50. Lessard, J. J. et al. Switching frontal polymerization mechanisms: FROMP and FRaP. *ACS Macro Lett.* **11**, 1097–1101 (2022).
51. Gao, Y. et al. Frontal polymerization of thin layers on a thermally insulating substrate. *ACS Appl. Polym. Mater.* **4**, 4919–4927 (2022).
52. Pramanik, P., Das, S. K. & Halder, M. FRET-selective and ion-exchange responsive smart nano-GUMBOS from functionalized pyrene: first observation of excited state aggregation (excimer) inside crystalline nanoball. *J. Phys. Chem. C* **124**, 4791–4801 (2020).
53. Pramanik, P., Sahoo, R., Das, S. K. & Halder, M. Fabrication of a GUMBOS-based acid-base indicator: smart probe for sensing acids and bases in any solvent. *Phys. Chem. Chem. Phys.* **22**, 28045–28054 (2020).

## Acknowledgements

Thanks to the entire REMAT EFRC team for valuable discussion and feedback over the course of this work. Thanks to Nick Monk, Harrison Root, Hayden Fowler and Patti Sawyer for assistance and instrument maintenance. Thanks to Dorothy Loudermilk, SCS Graphic Services, University of Illinois Urbana-Champaign for assistance with graphic design. This work was supported as part of the center for Regenerative Energy-Efficient Manufacturing of Thermoset Polymeric Materials (REMAT), an Energy Frontier Research Center funded by the U.S. Department of Energy, Office of Science, Basic Energy Sciences at the University of Illinois, Urbana-Champaign under award #DE-SC0023457 and at Sandia National Laboratories under contract DE-NA-0003525. S.R. was supported by an appointment to the National Nuclear Security Administration Minority Serving Institutions Internship Program (NNSA-MSIIP), sponsored by the U.S. Department of Energy and administered by the Oak Ridge Institute for Science and Education. Sandia National Laboratories is a multimission laboratory managed and operated by National Technology & Engineering Solutions of Sandia, LLC, a wholly owned subsidiary of Honeywell International Inc., for the U.S. Department of Energy's National Nuclear Security Administration under contract DE-NA0003525. This paper describes objective technical results

and analysis. Any subjective views or opinions that might be expressed in the paper do not necessarily represent the views of the U.S. Department of Energy or the United States Government.

## Author contributions

D.D. and A.G. designed and performed experiments, collected and analyzed data and interpreted results, contributed first drafts of the manuscript and contributed to manuscript revisions and editing. R.B. performed additional experiments, collected and analyzed data and interpreted results and contributed to manuscript revisions and editing. D.F. performed synthesis and NMR characterizations, analysis and interpretation of results and contributed to manuscript revisions and editing. V.R., A.J. and S.G. assisted with experiments and collected and analyzed data. S.R. assisted with data analysis, compilation and data archiving. J.M. provided guidance and critical feedback and contributed to the manuscript revisions and editing. S.L. and L.A. conceived the idea, directed the research, provided guidance and critical feedback, analyzed data and interpreted results and wrote the final manuscript, with contributions from all others.

## Competing interests

A non-provisional patent application has been filed by LA, SL, AG, and DD on the work described (Application #19/220,321). The authors RB, VR, DF, AJ, SG, SR and JM declare no competing interests.

## Additional information

**Supplementary information** The online version contains supplementary material available at <https://doi.org/10.1038/s41467-025-61484-9>.

**Correspondence** and requests for materials should be addressed to S. C. Leguizamón or L. N. Appelhans.

**Peer review information** *Nature Communications* thanks N. Gabriel Lemcoff and the other, anonymous, reviewers for their contribution to the peer review of this work. A peer review file is available.

**Reprints and permissions information** is available at <http://www.nature.com/reprints>

**Publisher's note** Springer Nature remains neutral with regard to jurisdictional claims in published maps and institutional affiliations.

**Open Access** This article is licensed under a Creative Commons Attribution-NonCommercial-NoDerivatives 4.0 International License, which permits any non-commercial use, sharing, distribution and reproduction in any medium or format, as long as you give appropriate credit to the original author(s) and the source, provide a link to the Creative Commons licence, and indicate if you modified the licensed material. You do not have permission under this licence to share adapted material derived from this article or parts of it. The images or other third party material in this article are included in the article's Creative Commons licence, unless indicated otherwise in a credit line to the material. If material is not included in the article's Creative Commons licence and your intended use is not permitted by statutory regulation or exceeds the permitted use, you will need to obtain permission directly from the copyright holder. To view a copy of this licence, visit <http://creativecommons.org/licenses/by-nc-nd/4.0/>.

© The Author(s) 2025